AIAA SciTech Forum
6-10 January 2025, Orlando, FL
AIAA SCITECH 2025 Forum

10.2514/6.2025-0264

Integrated Guidance and Control of Generic Hypersonic Glide Vehicles Using Computational Fluid Dynamics

Darryl J. Williams *, Diganta Bhattacharjee †, Travis W. Drayna ‡ , Maziar S. Hemati §, and Graham V. Candler ¶
University of Minnesota, Minneapolis, Minnesota, 55455

Matt Bartkowicz‖
GoHypersonic Inc, Minneapolis, Minnesota, 55413

Hypersonic glide vehicles (HGVs) encounter a wide range of speeds and extreme thermal environments; this creates complex flow fields that make guidance and control challenging. Rapid modeling of a glider's aerodynamic performance often relies on limited data-driven or empirical models. However, these models frequently overlook critical physics and necessary couplings, limiting their applicability and generalizability to new aerodynamic shapes. With modern advancements in numerical methods and computational hardware, high-fidelity computational fluid dynamics (CFD) has become a practical tool for rapidly generating data for HGVs and reducing uncertainties in control-related dynamics. In this work, an integrated guidance and control framework using a linear time-varying model predictive controller (LTV-MPC) has been applied to a generic HGV, with aerodynamic loads computed using CFD to capture the complex flow physics. An expansive aerodynamic database was rapidly generated, revealing that scaling the aerodynamic data by dynamic pressure yielded good agreement within the glide regime for moderate angles of attack and control surface deflections. Two quasi-equilibrium glide trajectories are evaluated in our simulations, 1) a trajectory featuring a pull-up maneuver, and 2) a trajectory maintaining constant dynamic pressure. In both cases, the proposed framework achieves adequate tracking performance, demonstrating its nominal robustness. This is notable as the LTV-MPC operates using linear models, yet the control inputs that it synthesizes are successfully applied to the nonlinear dynamics of the vehicle. This research supports ongoing efforts in multi-disciplinary design and optimization (MDAO) of hypersonic systems at the University of Minnesota. Significant progress has been achieved in developing rapid geometry and mesh generation techniques for parametrically defined geometries. Additionally, mesh deformation plugins have been integrated into the US3D CFD framework, facilitating the efficient generation of hypersonic flow fields for varying control surface deflections on complex geometries.

I. Introduction

Hypersonic glide vehicles (HGVs) are distinguished by the very high speeds they encounter while maneuvering within the Earth's atmosphere. The trajectory typically involves a descent through the less dense upper atmosphere, followed by a pull-up maneuver in denser regions. These vehicles are initially boosted to speeds exceeding Mach 5 in the upper atmosphere before entering the glide phase, which is the primary focus of this manuscript. During the glide phase, maneuvering is achieved using aerodynamic forces to adhere to path, structural, and thermal constraints while progressing toward a target. Due to prolonged high-speed flight within the atmosphere, HGVs experience significant integrated heat loads, necessitating a thermal protection system (TPS). While integrated heating effects are important to compute accurate aerodynamic forces, this study assumes that the heat flux from the flow to the TPS surface is balanced by the radiative flux away from the surface.

The maneuverability of HGVs exposes them to varied flight conditions along their trajectory, further complicated by high speeds, high enthalpies, and the transition to turbulence. Therefore, controls are essential for executing maneuvers

*Graduate Research Assistant, Department of Aerospace and Engineering Mechanics
†Postdoctoral Associate, Department of Aerospace and Engineering Mechanics, AIAA Member
‡Research Professor in Hypersonics, Department of Aerospace and Engineering Mechanics
§Associate Professor, Department of Aerospace and Engineering Mechanics, AIAA Associate Fellow.
¶McKnight Presidential Endowed Professor, Department of Aerospace and Engineering Mechanics, AIAA Fellow.
‖Senior Engineer

according to guidance laws or tracking nominal trajectories. For example, at high altitudes and Mach numbers, HGVs may experience thick boundary layers due to inviscid-viscous interactions and low dynamic pressures, diminishing the effectiveness of control surfaces. Additionally, flow separation during high control surface deflections or changes in angles of attack can further degrade control efficacy. These complexities highlight the importance of accurate simulations of the relevant physics for successful HGV design and operation.

Previous studies related to guidance and control of hypersonic vehicles in the existing literature have mainly relied on empirical data or simplified physics to evaluate hypersonic vehicle aerodynamics [1–6]. However, these methods are not generalizable to new geometries and may overlook critical flow phenomena, potentially leading to erroneous conclusions. Furthermore, the majority of guidance design in the existing literature are based on three degree of freedom (DOF) models considering both longitudinal and lateral motion [7–9], whereas existing control design strategies are largely based on two DOF longitudinal dynamical models of the vehicle [3–6]. Moreover, it is noteworthy that while most of the guidance formulations focus on unpowered gliding trajectories, control designs almost always assume that the vehicle can produce thrust. In the present study, we focus on gliding entry/re-entry missions without thrust, thereby rendering most of the existing control strategies difficult to adapt to our study. It is also not trivial to modify these existing control frameworks to be employed for a gliding flight since thrust plays an integral role in the design. Thus, there is a pressing need for developing *integrated guidance and control frameworks to generate and fly gliding trajectories representative of realistic conditions*.

Some of the first studies on integrated guidance and control can be found in [8, 10, 11]. These methods are formulated based on a linearization of the governing system around the desired trajectory, which is similar to the formulation we have pursued. However, the underlying assumption is that the bank angle and angle of attack are the 'control variables', which is not a realistic scenario. In reality, these are states of the vehicle which can potentially be modified through appropriate control inputs (e.g., elevator/elevon deflection for controlling the angle of attack). Recently, Shou et al. [12] introduced an integrated guidance and control formulation with fuel-to-air ratio and elevator deflection as the control inputs. The overall objective is to drive the velocity and altitude of the vehicle to specific desired values while satisfying constraints on the magnitude of fuel-to-air ratio. The guidance and control is integrated by generating the trajectory in the guidance module with the constraints. Tracking control is then designed using an adaptive backstepping approach. However, the simulation results in [12] show that although the constraints on the fuel-to-air ratio is satisfied, the controller demands large elevator deflections which is unconstrained (see Fig. 6 in [12]).

In this paper, we primarily focus on developing an integrated guidance and control framework for HGVs flying a typical boost glide trajectory. We consider the longitudinal motion of the vehicle with the aerodynamic loads computed through high-fidelity CFD for a fixed geometry. The vehicle geometry considered in this study is chosen to represent a generic HGV. We assume rigid body motion and neglect transient effects. Automated geometry and grid generation tools were employed for a parametrically defined HGV, and mesh deformation techniques were utilized to simulate control surface deflections during CFD evaluations. Therefore, the CFD generated flow fields explicitly incorporate the effects of control surfaces, ensuring accurate modeling of the HGV's motion. This work is part of a broader effort toward the Multi-disciplinary Design and Optimization of hypersonic systems, with HGVs serving as a case study. To mitigate the computational expense associated with the small temporal discretization required by the controller for HGV trajectories, an aerodynamic database derived from CFD was used instead. Future work aims to implement a closed-loop framework that directly integrates CFD evaluations instead of interpolating from an aerodynamic database.

In this work, given the current altitude and speed of the HGV, the guidance module computes the associated reference values in angle of attack, flight path angle, pitch rate, and elevator/elevon deflection. These reference states correspond to quasi-equilibrium gliding conditions for the HGV. A linear time-varying (LTV) model predictive control (MPC) framework is designed to track these references generated by the guidance module, while respecting the hard constraints on the deflection angle magnitude. This is achieved by solving a strictly convex quadratic program at every time instant to compute the commanded elevator/elevon deflections. The proposed framework is tested in numerical simulations representative of a nominal HGV's glide trajectory. Our results show that the proposed framework is able to successfully fly the vehicle along a given altitude profile despite initial errors in the altitude as well as other variables describing the motion. Moreover, the framework is successfully employed to glide at a constant dynamic pressure. Note that the MPC is based on LTV models and we have implemented the controller to simulate the nonlinear HGV dynamics. Therefore, these results showcase the nominal robustness of the MPC framework.

The paper is organized as follows: Section II outlines the methodology, including the generation and deformation of HGV geometries and meshes, the fluid solver used for generating the aerodynamic database, the equations of motion used in simulating the dynamics, and the integrated guidance and control framework. Section III presents the aerodynamic database results, followed by Section IV, which demonstrates the performance of the LTV-MPC framework during

a pull-up maneuver and a constant dynamic pressure glide. Finally, Section V summarizes the findings and outlines directions for future research.

II. Methodology

A. Geometry and meshing

The mesh generation tools and US3D plugins used in this work are described below.

1. CrossLink

The CrossLink software was initially developed at Los Alamos National Laboratory to support the NNSA Stockpile Stewardship Program. It is now being advanced by the University of Minnesota's National Hypersonic Research Group to enhance geometry and mesh generation for a wide range of hypersonic applications. The software employs a topology-based mesh generation approach and provides scalable capabilities through the use of high-order basis functions [13]. It features a Python API for geometry creation and supports mesh refinement to handle complex geometries with significant variation. CrossLink is also tailored to generate meshes for both fluid and structural regions in hypersonic test articles and vehicles.

2. Link3D

Grid generation was automated using LINK3D, a parallel topology-based mesh generation software developed by GoHypersonic, Inc [14]. In a topology based grid generation approach, the multi-block topology is initially sketched to fill the volume, and the exposed block boundaries are assigned to geometry groups. The LINK3D grid smoothing engine then refines the grid while ensuring that the boundaries align with the assigned geometry. Once a baseline topology, or reference topology, is created, it can be applied to any geometry within the parametric family for which it was designed. This topology-based method allows for the automatic generation of high-quality hexahedral grids to accommodate changes to the surface of the mesh.

3. US3D Multi-mesh Plugin

In scenarios where geometries, flow conditions, and boundary conditions evolve dynamically, efficiently generating computational grids is critical. Static grids are often inadequate for problems requiring high accuracy in regions with rapid geometric changes or across vastly different parameter spaces. Additionally, creating static grids demands significant effort and domain expertise, redirecting resources from data generation to grid creation. The Multi-Mesh tool addresses these challenges by enabling adaptive grid interpolation and management across varying parameters such as Mach number, angle of attack, and rotational motion.

The Multi-Mesh plugin is a framework designed to streamline simulations involving geometries with well-defined, parametric definitions. It supports multi-parameter mesh transformations, allowing more than one parameter to define the geometry. New grids are quickly generated using Non-Uniform Rational B-Splines (NURBS) for interpolation. With a Fortran-based backend and Python interfaces, the tool provides a robust and scalable platform for applications such as aerodynamics and fluid-structure interactions. Key use cases include trajectory simulations and as highlighted in this manuscript, the rapid creation of aerodynamic databases.

The Multi-Mesh plugin integrates seamlessly with the US3D flow solver. It employs NURBS interpolation for dynamic transformations and features a modular design for compatibility with Python workflows or compiled Fortran plugins. NURBS-based interpolation is used to compute control point meshes from the input anchor meshes. NURBS interpolation uses weights defined by the *knot vector* (which defines the non-uniform spacing of the meshes in the parametric space) and the degree of interpolation. For each parameter, interpolation is done by creating a linear system of basis function weights to compute control points orthogonal to that parameter. This is done for each parameter, with subsequent parameters interpolating through the control point result of the previous parameter. The tensor product result of each parameter interpolation that gives the final result is a symmetric operation, meaning the result is unique and not dependent on the ordering of the parameters.

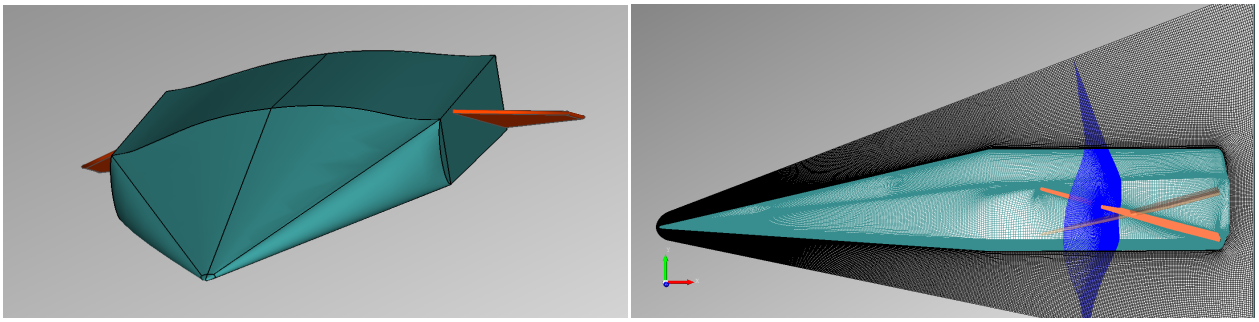

(a) +15° full-body geometry **(b) superimposed ±15° deflection for glider**

Fig. 1 Mesh and geometry of the generic HGV used. Geometry was created using CrossLink's python API while the grid was generated using Link3D.

B. Flow Solver

To evaluate the aerodynamic forces and moments outlined in Equation 1 (see section C, below), we use flow fields generated by the US3D CFD solver. US3D [15] is an unstructured finite-volume code that approximately solves the weak form of the compressible Navier-Stokes equations. In this work, for simplicity, we make the assumption that the fluid is a perfect gas, and that the flow is laminar. These assumptions are made to reduce the computational cost associated with generating over 6,000 flowfields required for this study. It should be noted that precise aerothermodynamic settings and advanced fluid dynamics modeling aspects, which are essential for more realistic simulations, are beyond the scope of this work.

The fluid domain assumes symmetry along the vehicle's centerline. For each run, we drive the solution to a steady state using a hybrid DPLR-FMPR first-order implicit method [16]. Its construction and numerics enable rapid convergence of flow fields by leveraging the strong directionality of the physics in the high aspect ratio elements near walls, (these are needed to resolve the thin boundary layers along the vehicle surface). The boundary conditions consist of supersonic inflow and outflow, with a symmetry boundary condition applied along vehicle's centerline (in the x-y plane). Furthermore, we assume radiative equilibrium with an emissivity of $\epsilon = 0.85$.

The primary focus here was to demonstrate the control of generic HGVs with control surfaces during its glide phase. As a result, data was generated for plausible flight conditions. We used the following parameter ranges:

- $\delta \in \{-10, -9, \ldots, 14, 15\}^\circ$
- $\alpha \in \{-5, -4, \ldots, 19, 20\}^\circ$
- $V_\infty \in \{2.0, 2.5, 3.0\}$ km/s
- $\rho_\infty \in \{1.8410 \cdot 10^{-2}, 8.4634 \cdot 10^{-3}, 3.9957 \cdot 10^{-3}\}$ kg/m^3

Where δ is the fin deflection, α is the angle of attack, V_∞ is the free stream velocity, and ρ_∞ is the free stream density. The selected densities correspond to the altitudes of 30, 35, and 40 km, as defined by the standard atmospheric model [17].

The multi-mesh framework described in Section II.A.3 was used to interpolate between anchoring meshes for each fin deflection. Integration with US3D for aerodynamic database generation is outlined in Algorithm 1.

C. HGV Integrated Guidance and Control

1. *Dynamical Model of Longitudinal Dynamics*

The longitudinal dynamics of an HGV is given by a set of ordinary differential equations as follows:

$$\begin{aligned} \dot{V} &= -\frac{D}{m} - g \sin\gamma \\ \dot{\alpha} &= q - \frac{L}{mV} + \frac{g}{V}\cos\gamma \\ \dot{\gamma} &= \frac{L}{mV} - \frac{g}{V}\cos\gamma \\ \dot{q} &= \frac{\tau_y}{I_y} \end{aligned} \tag{1}$$

Algorithm 1: CFD Aero-database Generation

Initialization: Given the lower and upper limits of (α, h, V, δ), define a 4-d hypercube.
Set: `Mass` = 1000 (mass of vehicle), `nevals` = 1800 (number of CFD time steps), and `nit` = 0 (iteration counter).
while *Aero-database is not complete* **do**
  Update Inflow:
    Input: (α, h, V)
    Output: ρ, updated inflow conditions
    Call `atmospheric_model(`h`)` to compute ρ, T (e.g., using Standard 1976 or exponential atmospheric models).
    Call `reset_BC(`V, ρ, α, T`)` to Update boundary conditions.
  Interpolate Mesh:
    Input: δ (control surface deflection)
    Output: Interpolated mesh configuration corresponding to δ
    Call `multi_mesh_interpolate(`δ`)` (as described in Section II.A.3).
  Compute CG and I_y:
    Input: Wall centroid locations
    Output: Center of gravity (CG) and moment of inertia (I_y)
    Call `compute_CG_and_I()` (accounting for fin deflection).
  Converge Aerodynamic Forces and Moments:
    while $nit \leq nevals$ **do**
      `cfl` $\leftarrow \min(10,000.0, 1.2^{\texttt{nit}})$
      Perform CFD evaluation using `cfl`.
      Increment `nit`: `nit` $\leftarrow$ `nit` + 1.

where V is the speed, α is the angle of attack, γ is the flight path angle, q is the pitch rate, and I_y is the moment of inertia about the pitch axis of the HGV. Also, lift L, drag D and pitch moment τ_y are the aerodynamic loads, which are functions of the elevon or elevator deflection angle δ. Note that the dynamics in (1) is associated with the corresponding kinematics given by

$$\begin{aligned} \dot{R} &= V\cos\gamma \\ \dot{h} &= V\sin\gamma \end{aligned} \tag{2}$$

where R is the downrange distance, h is the altitude. For convenient notations, we will denote the nonlinear dynamics (1) in a compact form as

$$\dot{x} = f(x,u) \tag{3}$$

where $u = \delta$ denotes the control input, and $x \in \mathbb{R}^4$ and $f : \mathbb{R}^4 \times \mathbb{R} \to \mathbb{R}^4$ respectively denote the states and nonlinear dynamics, which are given by

$$x = \begin{bmatrix} V \\ \alpha \\ \gamma \\ q \end{bmatrix}, f(x,u) = \begin{bmatrix} -\frac{D}{m} - g\sin\gamma \\ q - \frac{L}{mV} + \frac{g}{V}\cos\gamma \\ \frac{L}{mV} - \frac{g}{V}\cos\gamma \\ \frac{\tau_y}{I_y} \end{bmatrix}$$

2. Guidance Computation

The main role of the guidance module in the present study is to generate reference states $x_r(t) = \begin{bmatrix} V_r(t) & \alpha_r(t) & \gamma_r(t) & q_r(t) \end{bmatrix}^{\mathrm{T}}$ and reference control $u_r(t) = \delta_r(t)$ trajectories such that the HGV tracks a specified or reference altitude profile $h_r(t)$. The altitude profile is assumed to be at least continuously differentiable and we assume that $\dot{h}_r(t)$ is available to the guidance module. It is assumed here that the mission requirements are enforced through the specified altitude profile. For the reference speed and pitch rate, we set $V_r(t) = V(t)$ and $q_r(t) = 0$. These

choices mean that (a) the speed is allowed to vary according to the vehicle dynamics and we do not explicitly control the speed variation; (b) the pitch rotations are ideally kept at a minimum. The reference values in the flight path angle are specified so that the altitude tracking error goes to zero, i.e., $h(t) \to h_r(t)$. Therefore, inspired by the concept of sliding mode control [18], we set the $\gamma_r(t)$ as

$$\gamma_r(t) = \arcsin\left(\frac{\dot{h}_r(t) - k_1\Delta h(t) - k_2\text{sgn}(s(t))}{V(t)}\right) \tag{4}$$

where k_1, k_2 are positive constants, $\Delta h(t) = h(t) - h_r(t)$ is the altitude tracking error, and $s(t) = \Delta h(t) + k_1 \int_{t_0}^{t} \Delta h(t)dt$ is the sliding variable, and $\text{sgn}(s)$ is the signum function given by

$$\text{sgn}(s) = \begin{cases} -1 & \text{if } s < 0, \\ 0 & \text{if } s = 0, \\ +1 & \text{if } s > 0. \end{cases} \tag{5}$$

A major drawback of the sliding mode control is the issue of chattering [18] as the function $\text{sgn}(s)$ is discontinuous at $s = 0$. There are several ways to deal with this issue. One of the standard ways to alleviate the issue of chattering is by introducing a continuous approximation of the signum function as [19]

$$\text{sgn}(s(t)) \approx \frac{2}{\pi}\arctan(\mu_s s(t)) \tag{6}$$

where $\mu_s > 0$ is a positive constant and the approximation error can be minimized by increasing the magnitude of μ_s. Finally, the $(\alpha_r(t), \delta_r(t))$ pair is computed by solving the following two equations

$$\frac{L}{mV} - \frac{g}{V}\cos\gamma \quad = 0 \tag{7}$$

$$\frac{\tau_y}{I_y} \quad = 0 \tag{8}$$

Thus, the $(\alpha_r(t), \delta_r(t))$ with $q_r(t) = 0$ is equivalent to finding an equilibrium in the rotational DOF (i.e., pitch rotation).

3. Control Design: LTV-MPC

The LTV-MPC approach involves linearizing the governing system in (3) about the reference trajectory (x_r, u_r) for the entire duration of the mission. We start by performing a Taylor expansion of the nonlinear function about (x_r, u_r), which leads to the following:

$$\dot{x} = f(x_r, u_r) + \frac{\partial f}{\partial x}\Big|_{(x,u)=(x_r(t),u_r(t))}(x - x_r) + \frac{\partial f}{\partial u}\Big|_{(x,u)=(x_r(t),u_r(t))}(u - u_r) + w(x, x_r, u, u_r) \tag{9}$$

where all the higher order terms are absorbed in $w(x, x_r, u, u_r)$. Define the following quantities as

$$\Delta x = x - x_r, \Delta u = u - u_r, A(t) = \frac{\partial f}{\partial x}\Big|_{(x,u)=(x_r(t),u_r(t))}, B(t) = \frac{\partial f}{\partial u}\Big|_{(x,u)=(x_r(t),u_r(t))}. \tag{10}$$

Now, the linearized dynamics in (9) can be equivalently expressed as

$$\Delta\dot{x} = A(t)\Delta x + B(t)\Delta u + w(t) \tag{11}$$

where $w(t)$ can be treated as a time-varying disturbance. Note that the linear time-varying system (11) governs the local dynamic behavior of the HGV around the time-varying reference trajectory. The system (11) can be discretized (e.g., using Euler discretization) and expressed as

$$\Delta x(k+1) = A_d(k)\Delta x(k) + B_d(k)\Delta u(k) + w(k) \tag{12}$$

where $k \in \mathbb{Z}_{\geq 0}$ denotes the discrete time steps with $\mathbb{Z}_{\geq 0}$ as the set of non-negative integers. The MPC formulation given in Ref. [20] is adopted here, with appropriate modifications to obtain a full-state feedback design for the time-varying

system. Note the disturbances are assumed to be identically zero for the prediction equations of the MPC. It should also be noted that we don't assume time-variation within the prediction horizon of the MPC which results in an optimization with reduced computational complexity [21, 22]. This simplifying assumption can be further justified by choosing the discretization time-step and prediction horizon to be sufficiently small so that the underlying system does not evolve drastically during the prediction. Therefore, the prediction equations at a time-step k are given in a compact form as

$$\Delta X(k) = F(k)\Delta x(k) + H(k)\Delta U(k), \tag{13}$$

where

$$\Delta X(k) = \begin{bmatrix} \Delta x(k) \\ \Delta x(k+1) \\ \Delta x(k+2) \\ \cdot \\ \cdot \\ \cdot \\ \Delta x(k+N-1) \end{bmatrix}, \ \Delta U(k) = \begin{bmatrix} \Delta u(k) \\ \Delta u(k+1) \\ \Delta u(k+2) \\ \cdot \\ \cdot \\ \cdot \\ \Delta u(k+N-1) \end{bmatrix}, F(k) = \begin{bmatrix} I \\ A_d(k) \\ A_d^2(k) \\ \cdot \\ \cdot \\ \cdot \\ A_d^{N-1}(k) \end{bmatrix},$$

$$H(k) = \begin{bmatrix} O & \cdot & \cdot & \cdot & \cdot & O \\ B_d(k) & \cdot & \cdot & \cdot & \cdot & O \\ A_d(k)B_d(k) & B_d(k) & \cdot & \cdot & \cdot & O \\ A_d^2(k)B_d(k) & A_d(k)B_d(k) & B_d(k) & \cdot & \cdot & O \\ \cdot & \cdot & \cdot & \cdot & \cdot & \cdot \\ \cdot & \cdot & \cdot & \cdot & \cdot & \cdot \\ A_d^{N-2}(k)B_d(k) & A_d^{N-3}(k)B_d(k) & \cdot & \cdot & B_d(k) & O \end{bmatrix}$$

where I and O are identity and null matrices of appropriate dimensions, respectively, and N is the prediction or control horizon. The prediction and control horizons are considered equal for this present formulation. The terminal state is given by

$$\Delta x(k+N) = A_d^N(k)\Delta x(k) + \bar{B}_d(k)\Delta u(k) \tag{14}$$

where $\bar{B}_d(k) = \begin{bmatrix} A_d^{N-1}(k)B_d(k) & A_d^{N-2}(k)B_d(k) & \cdot & \cdot & \cdot & A_d(k)B_d(k) & B_d(k) \end{bmatrix}$.

MPC is a finite-horizon optimal control strategy and it allows the user to specify a cost (or objective) function, which typically gets minimized, to calculate the optimal solution after each sampling interval or discretization time-step. The choice of the cost function should be such that minimizing it corresponds to control objective satisfaction with the least possible control effort. In this case, the control objective is regulation, i.e., we want to drive the predicted states in (13) to the origin, i.e., $\Delta X(k) \to 0$. For the present formulation, we choose a cost function that penalizes the weighted norm of predicted state perturbations $\Delta X(k)$ and the weighted norm of predicted control input perturbations $\Delta U(k)$. Therefore, the quadratic cost function for the LTV-MPC is given by

$$J(\Delta X(k), \Delta x(k+N), \Delta U(k)) = \Delta X^{\mathrm{T}}(k)\bar{Q}_N\Delta X(k) + \Delta U^{\mathrm{T}}(k)\bar{R}_N\Delta U(k) + \Delta x^{\mathrm{T}}(k+N)Q_f\Delta x(k+N) \tag{15}$$

where $Q_f \geq 0$, and the matrices $\bar{Q}_N$, and $\bar{R}_N$ are given by

$$\bar{Q}_N = \mathrm{diag}\,(Q, Q, \ldots, Q)\,, \bar{R}_N = \mathrm{diag}\,(R, R, \ldots, R)\,,$$

where Q and R are diagonal matrices with $Q \geq 0$ and $R > 0$. The matrix Q_f is chosen based on the solution to the discrete-time Algebraic Riccati Equation

$$P = A_d^{\mathrm{T}}(k)PA_d(k) - A_d^{\mathrm{T}}(k)PB_d(k)(R + B_d^{\mathrm{T}}(k)PB_d(k))^{-1}B_d^{\mathrm{T}}(k)PA_d(k) + Q. \tag{16}$$

Upon solving the above equation, we set $Q_f = P$. After substituting the expressions for $\Delta X(k)$ and $\Delta x(k+N)$ in (15), the cost function $J(\Delta X(k), \Delta x(k+N), \Delta U(k))$ can be equivalently expressed as a quadratic in $(\Delta x(k), \Delta U(k))$ as

follows

$$
\begin{aligned}
J(\Delta x(k), \Delta U(k)) = \Delta U^{\mathrm{T}}(k) \left[H^{\mathrm{T}}(k) \bar{Q}_N H(k) + \bar{R}_N + \bar{B}_d^{\mathrm{T}}(k) Q_f \bar{B}_d(k) \right] \Delta U(k) \\
+ 2 \left((F(k)\Delta x(k))^{\mathrm{T}} \bar{Q}_N H(k) + (A_d^N(k)\Delta x(k))^{\mathrm{T}} Q_f \bar{B}_d(k) \right) \Delta U(k) \\
+ (F(k)\Delta x(k))^{\mathrm{T}} \bar{Q}_N (F(k)\Delta x(k)) + (A_d^N(k)\Delta x(k))^{\mathrm{T}} Q_f (A_d^N(k)\Delta x(k)).
\end{aligned} \tag{17}
$$

Finally, we specify the input constraints as

$$
\Delta u_{\min}(k) 1_N \leq \Delta U(k) \leq \Delta u_{\max}(k) 1_N
$$

where 1_N stands for an N-dimensional vector of ones, $\Delta u_{\min}(k) = u_{\min} - u_r(k)$ and $\Delta u_{\max}(k) = u_{\max} - u_r(k)$ with $u_r(k)$ denoting the reference control input at the current time-step k. Therefore, the optimization problem to be solved for the LTV-MPC at each time-step k is given by

$$
\begin{aligned}
&\min_{\Delta U(k)} \; J(\Delta x(k), \Delta U(k)) \\
&\text{s.t. } \Delta u_{\min}(k) 1_N \leq \Delta U(k) \leq \Delta u_{\max}(k) 1_N
\end{aligned} \tag{18}
$$

which is a quadratic program (QP). In this work, MATLAB's QP solver 'quadprog' is utilized solve this QP. Once the QP in (18) is solved and we obtain the optimal solution $\Delta U^{\star}(k) = \begin{bmatrix} \Delta u^{\star}(k) & \Delta u^{\star}(k+1) & \Delta u^{\star}(k+2) & \dots & \Delta u^{\star}(k+N-1) \end{bmatrix}^{\mathrm{T}}$, the control input for the current time-step is chosen as $u(k) = u_r(k) + \Delta u^{\star}(k)$. This procedure is repeated to compute the deflection δ at every time-step. A summary of the proposed LTV-MPC-based algorithm for integrated guidance and control is outlined in Algorithm 2. For simplicity of the presentation here, we have assumed that the reference altitude and altitude rate profiles are known a-priori for the description of Algorithm 2. However, note that the proposed framework is amenable to scenarios where the reference altitude and altitude rate has to be generated at every time instant (see Section IV.B).

Algorithm 2: Integrated Guidance and Control of HGV: LTV-MPC

Initialization: Given the trajectory $(h_r(t), \dot{h}_r(t))$ for $t \in [t_0, t_f]$, select a discretization time-step Δt and set $t_k = t_0$ and $k = 0$. Choose $Q, R, N, k_1, k_2, \mu_s, u_{\min}, u_{\max}$.
while $t_k \leq t_f$ **do**
  Guidance Module
    Given $(h(t_k), \int_{t_0}^{t_k} \Delta h \, dt, h_r(t_k), \dot{h}_r(t_k), V(t_k))$, compute $(\alpha_r(t_k), \gamma_r(t_k), \delta_r(t_k))$.
    Set $x_r(t_k) = \begin{bmatrix} V(t_k) & \alpha_r(t_k) & \gamma_r(t_k) & 0 \end{bmatrix}^{\mathrm{T}}$, $u_r(t_k) = \delta_r(t_k)$.
  Controller Module
    Generate the continuous-time LTV model matrices $A(t_k), B(t_k)$ by linearizing $f(x, u)$ around $(x_r(t_k), u_r(t_k))$.
    Set $\Delta x(k) = x(t_k) - x_r(t_k)$.
    Discretize $A(t_k), B(t_k)$ to obtain $A_d(k), B_d(k)$.
    Solve the QP in (18) to compute $\Delta u^{\star}(k)$.
    Set $u(t_k) = u_r(t_k) + \Delta u^{\star}(k)$.
  HGV Motion
    Integrate the kinematics in (2) and dynamics in (3) from t_k to $t_k + \Delta t$ using $\delta(t_k) = u(t_k)$.
    Set $t_k = t_k + \Delta t$, $k = k + 1$.

III. Aerodynamic Database

A. Static Stability

The static stability analysis for the geometry was conducted using freestream conditions corresponding to an altitude of 35 km and a velocity of 2.5 km/s. The neutral point (χ_{np}), which is the location of zero pitching moment, was determined by evaluating the stability derivative $\frac{\partial M_y}{\partial \alpha}$, solving for χ_{np}, and using this to inform the mass distribution of

the vehicle to achieve an appropriate center of gravity location. Where M_y is the pitching moment. Note that in the following discussion, the subscript 'LE' refers to the leading edge; however, any arbitrary point can be selected.

Starting with a definition of the moment on the vehicle:

$$M_y = (M_y)_{LE} + xF_y, \tag{19a}$$

Where F_y is the total force over the vehicle in the y-direction and x is the perpendicular distance from the point 'LE' and the line formed by F_y. We take an analytical derivative with respect to the angle of attack:

$$\frac{\partial M_y}{\partial \alpha} = \frac{\partial (M_y)_{LE}}{\partial \alpha} + x\frac{\partial F_y}{\partial \alpha}, \tag{19b}$$

and set the derivative to zero to find the root:

$$0 = \frac{\partial (M_y)_{LE}}{\partial \alpha} + \chi_{np}\frac{\partial F_y}{\partial \alpha}, \tag{19c}$$

which gives the neutral point as:

$$\chi_{np} = -\frac{\partial (M_y)_{LE}}{\partial F_y}. \tag{19d}$$

The results of computing the neutral point from Equation (19d) as a function of (δ, α) are presented in Figure 2. These results are expressed as a percentage of the mean aerodynamic chord (MAC), denoted as $\bar{c}$.

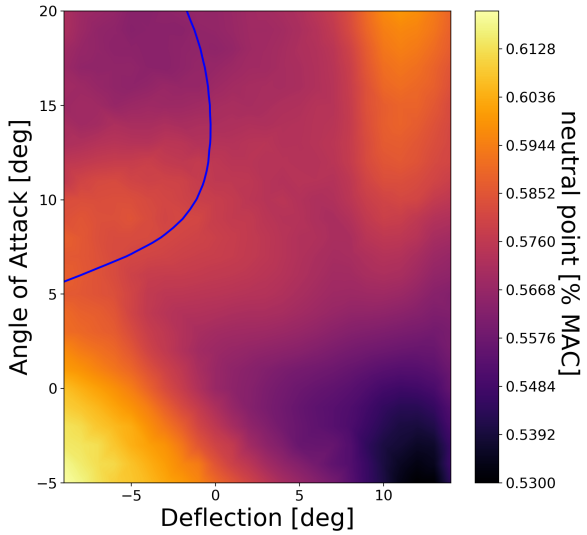

Fig. 2 Neutral point as a % of MAC for HGV going 2.5 km/s at 35 km. Blue line indicates zero pitch moment on the vehicle.

B. Aerodynamic Forces and Moments

The responses of the integrated quantities of lift, drag, and moments with respect to the angles of attack and fin deflections were consistent across the ranges considered. This is illustrated in Figure 3, where the coefficients of lift, drag, and moment are nearly identical within these ranges.

As a result, the aerodynamic quantities were extrapolated and interpolated by scaling with the dynamic pressure, $\bar{q}$. Discrepancies in the data were observed only at the extremes of fin deflections and angles of attack, indicating potential areas of additional physical concern and investigation, such as flow separation. A slice of the aerodynamic database at a specific altitude and speed is shown in Figure 4.

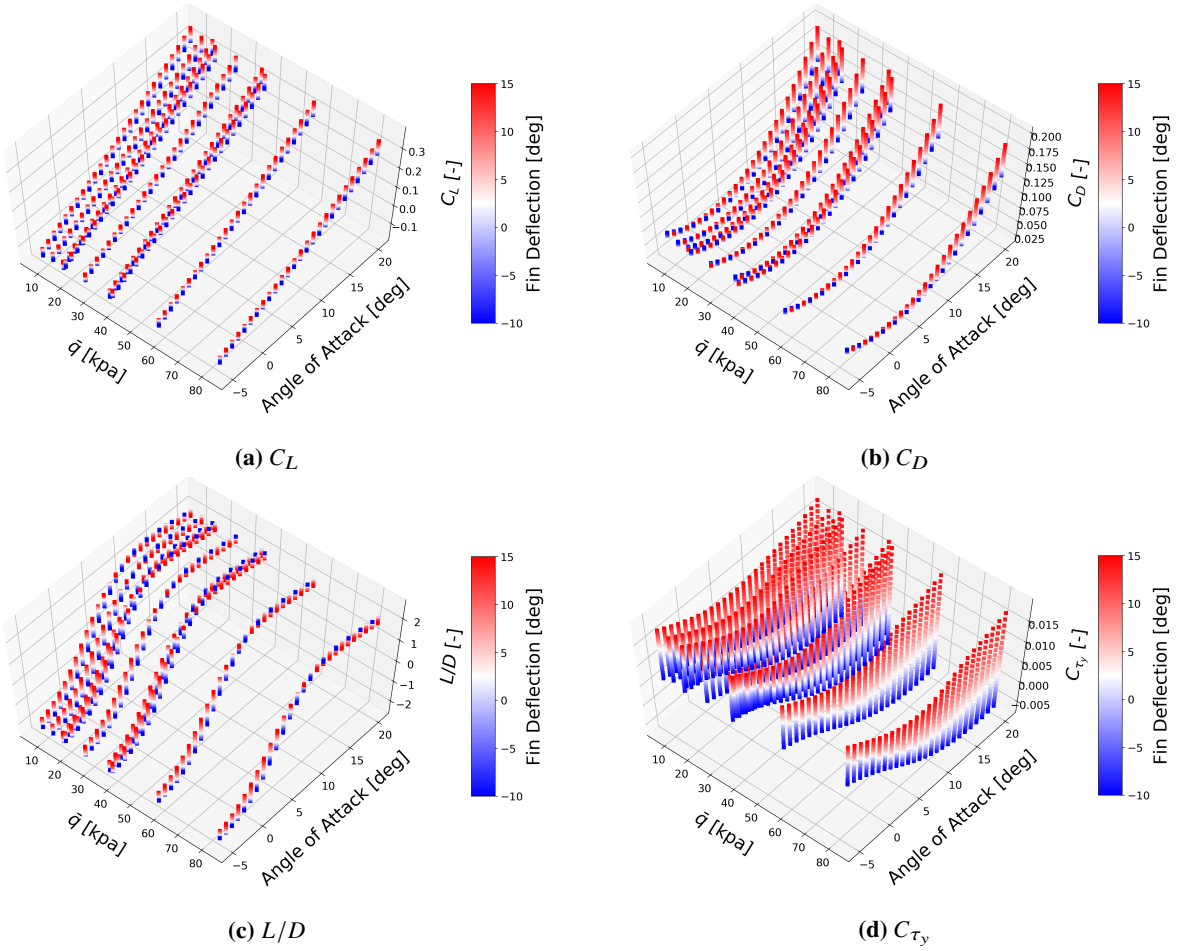

(a) C_L **(b)** C_D

(c) L/D **(d)** C_{τ_y}

Fig. 3 Scatter plot of all aerodynamic coefficients as a function of dynamic pressure and angle of attack, with the color mapping denoting fin deflection.

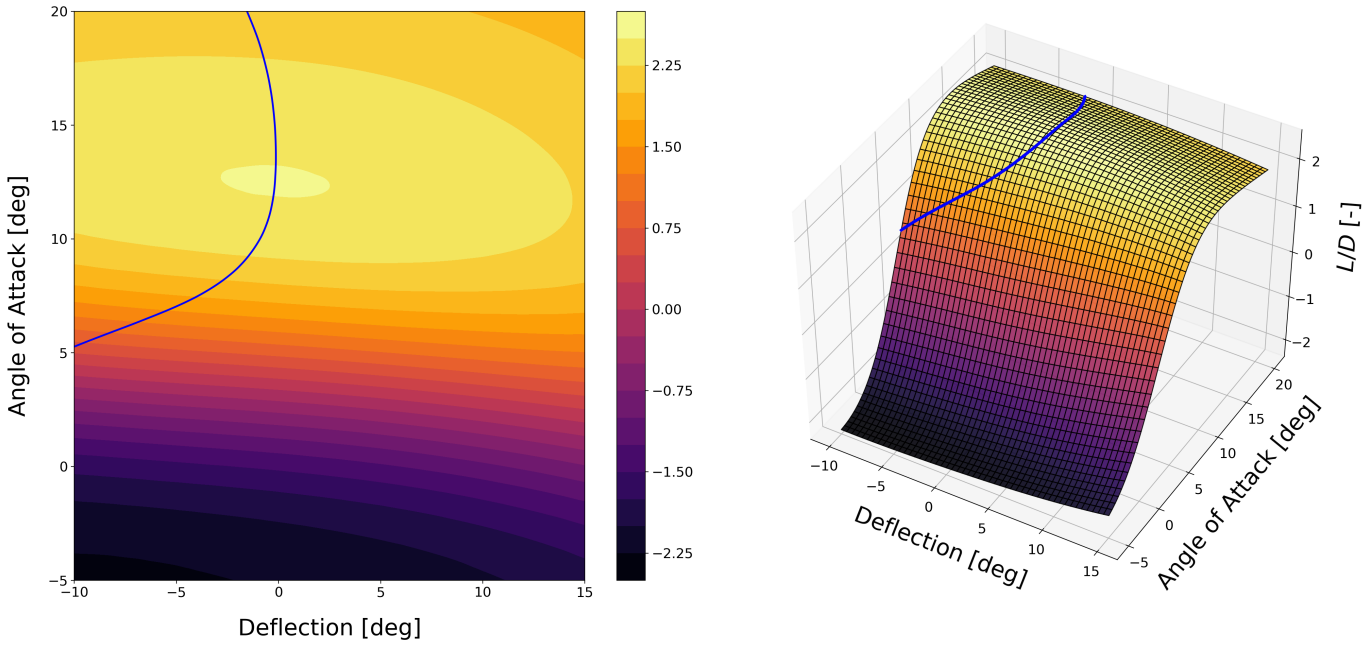

(a) L/D

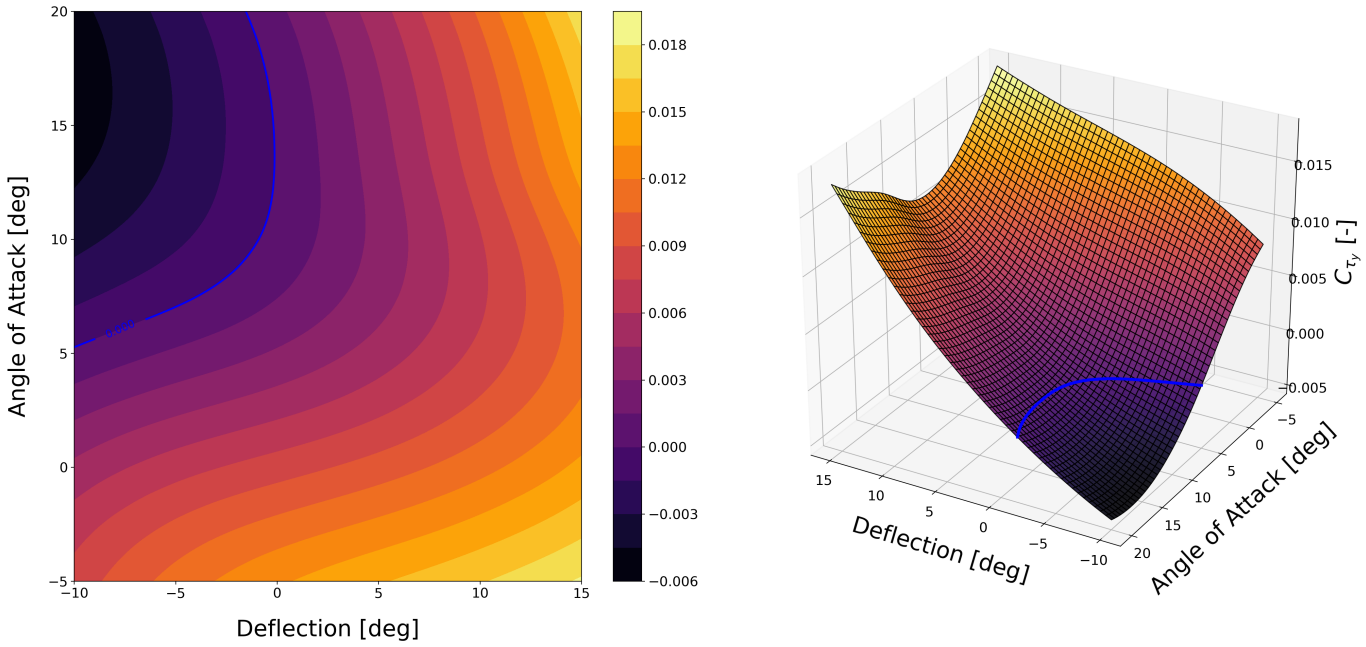

(b) moments

Fig. 4 Interpolated surface plot of pitch moments and L/D from the aerodynamic database at 2.5km/s and 30 km. The blue line indicates zero pitching moment on the vehicle.

C. The flowfield at Maximum L/D

We take a closer look at the flow field corresponding to max L/D. For us, this occurs at the trajectory point with $\alpha = 13°, \delta = 0°$, 30 km altitude, and a speed of 3 km/s. Key flow features of the vehicle at this condition are briefly discussed. Given that surface heating is a critical consideration in hypersonic vehicle design: the temperature distribution along the vehicle's geometry is shown in the upper right image of Figure 5. Close-ups of the control surfaces

are provided in the lower images of Figure 5, highlighting two notable flow features:

1) Shock-shock interactions between the shocks originating from the fin's leading edge and the nose.
2) Streaks along the fin's length in the x-direction evident in the temperature distributions (lower images of Figure 5).

These streaks coincide with the variations in heat flux and temperature along the fin's span in the z-direction (upper-left images of Figure 5). The location from which the upper-left image of Figure 5 was taken is at the truncation of the 60° swept fin, denoted by black lines in the lower images. Prior studies, such as by Knutson et al. [23], have examined the complexities of flow features on highly swept fins. Their findings show that horseshoe vortices and leading-edge vortices originate near the base of a control surface leading edge and can significantly influence lift, drag, and heat flux. These coherent structures also may promote transition to turbulence. To visualize these structures, the Q-criterion (the second invariant of the velocity gradient tensor) is used in Figure 6. It is noted that the vortical structures are under-resolved with a mesh consisting of 14 million elements. Despite this, the general formation of vortical structures near the base of the fin, traveling in the stream-wise direction and hugging the body, can be observed in Figure 6. The streaks observed in Figure 5 qualitatively align with the horse-shoe vortices originating from the fin's base. While the Q-criterion is employed to visualize vortical structures, it is not entirely effective. Much of the regions depicted in Figure 6 away from the fin-body junction represent areas of high shear stress rather than true vortices. Further analysis is necessary to refine and visualize these structures across the vehicle's body and fins and draw further conclusions.

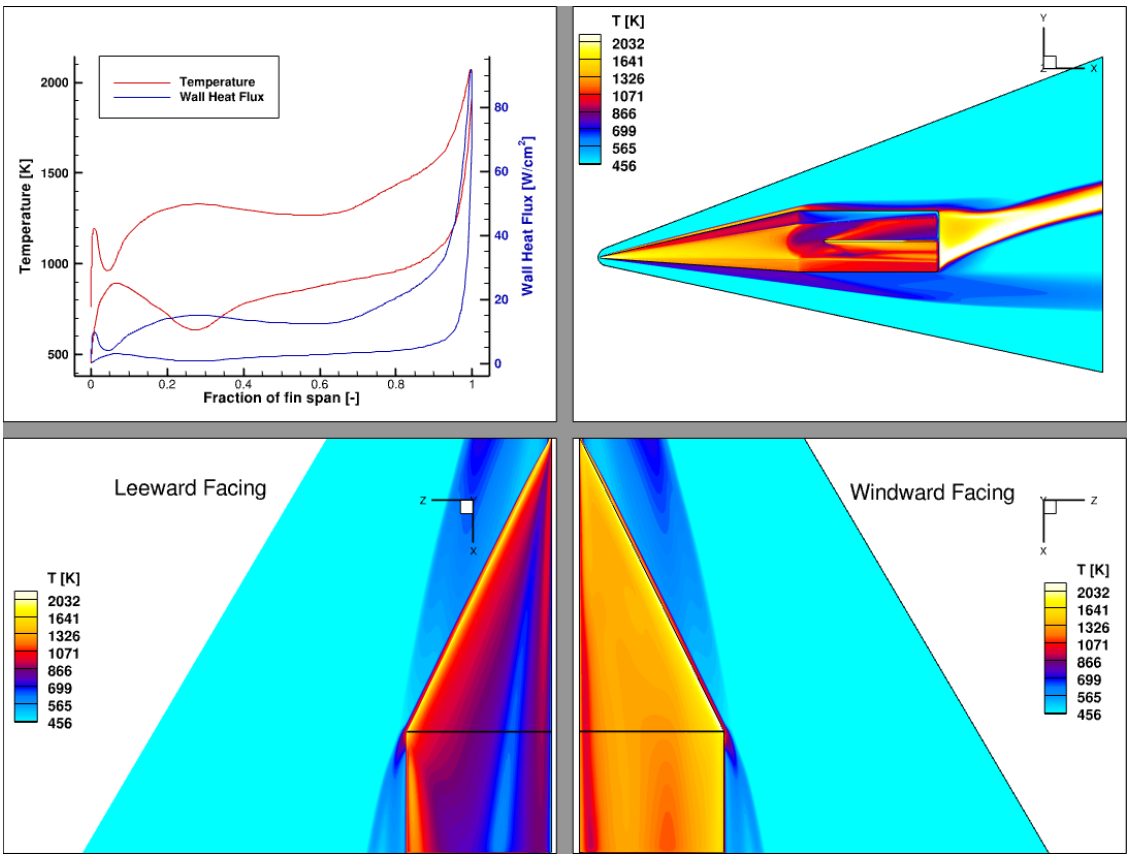

Fig. 5 Contour plot (upper-right) and line plot (upper-left) of temperature at max L/D conditions. The line plot represents temperature and heat flux over the non-dimensionalized span of the fin. The location where the line plot extracted data is denoted by black lines in the close-up view of the fin (lower images).

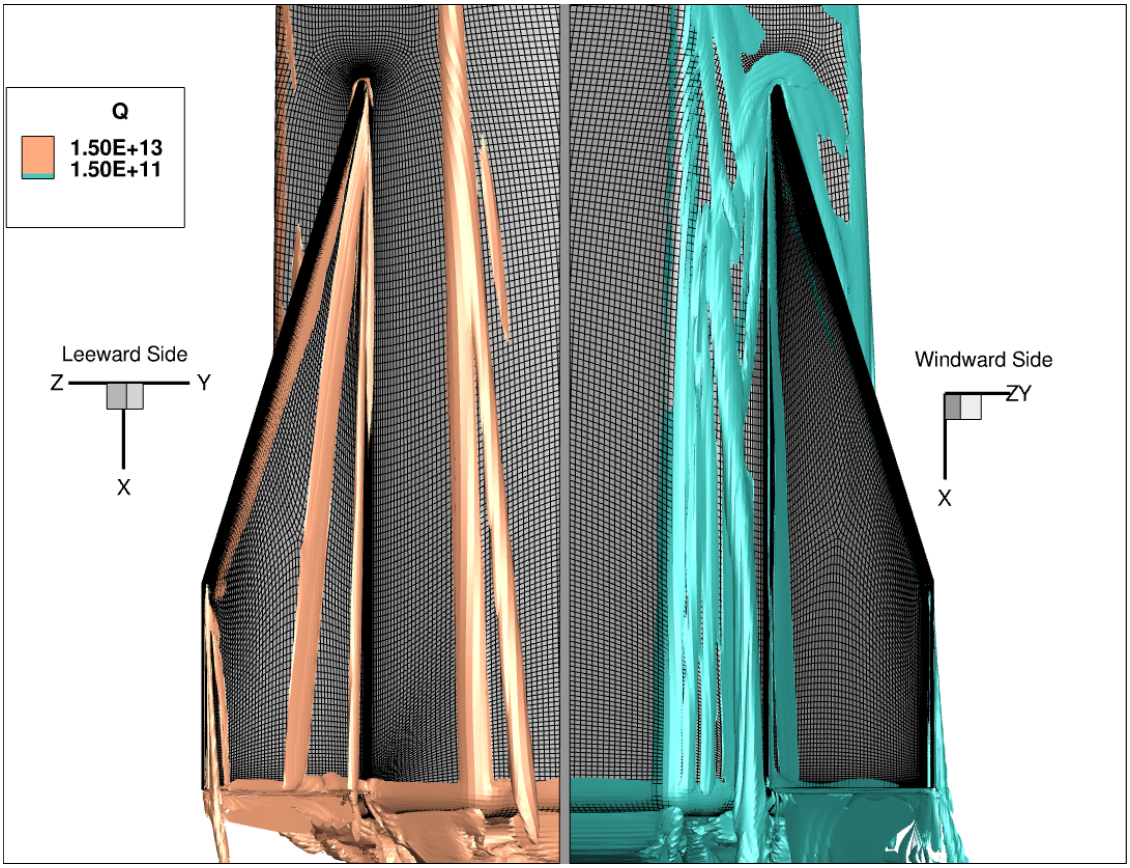

Fig. 6 Depiction of vortical structures at Max L/D conditions using Q-criteria Isosurfaces. The left image depicts the leeward side of the fin (partially hidden from the flow) while the right depicts the windward side (facing the flow).

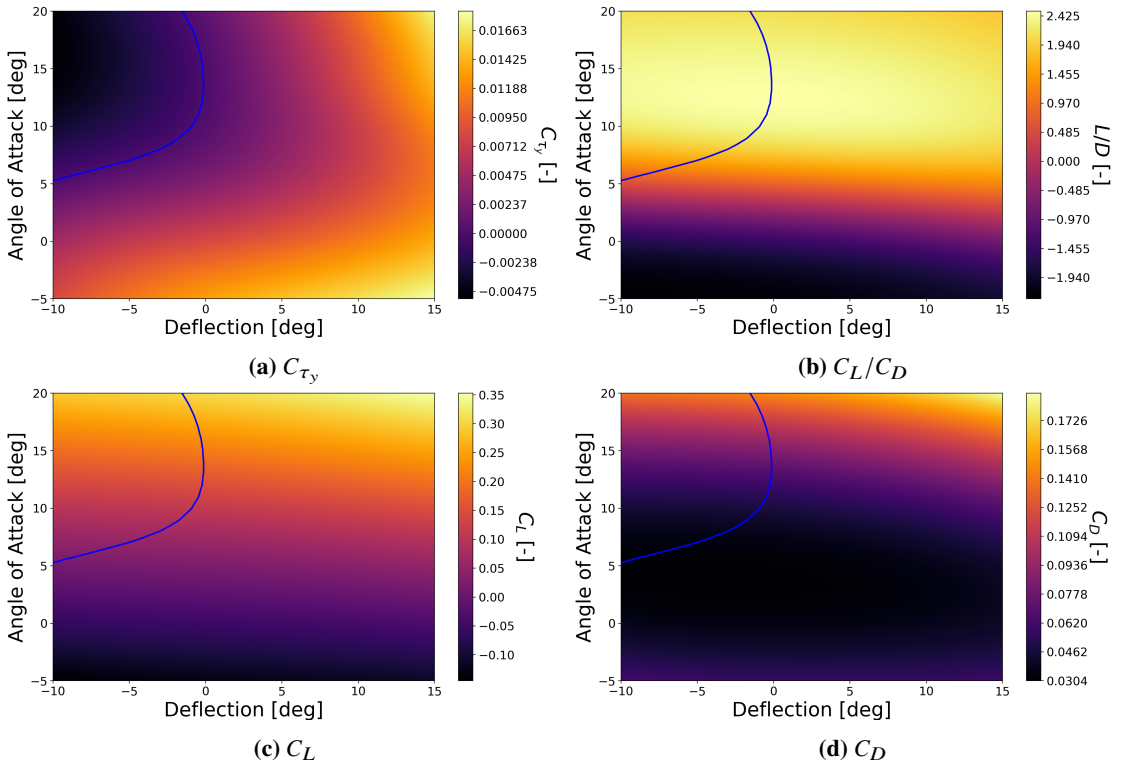

(a) C_{τ_y} **(b)** C_L/C_D

(c) C_L **(d)** C_D

Fig. 7 The aerodynamic load coefficients corresponding to $(h, V) = (30\ \textbf{km}, 2500\ \textbf{m/s})$**. Note that the blue line denotes the** $C_{\tau_y} = 0$ **or** $\dot{q} = 0$ **contour.**

IV. Numerical Simulation of HGV Flight

The relevant parameters for the vehicle geometry are as follows:

$$m = 1000\ \text{kg}, I_y = 247.2\ \text{kgm}^2, \bar{c} = 3.6\ \text{m}, S = 4.4\ \text{m}^2 \tag{20}$$

where $\bar{c}$ and S stand for mean aerodynamic chord and reference area, respectively. In terms of the aerodynamic database, we pick the aerodynamic forces and moments corresponding to a fixed pair of $(h, V) = (30\ \text{km}, 2500\ \text{m/s})$ and non-dimensionalize the forces and moments using the $\bar{c}$ and S given in (20). Note that these force and moment coefficients are utilized for the results shown in this section and the density variation is captured through an exponential atmospheric density model given by $\rho(h) = \rho_0 \exp(-a_h h)$ where $\rho_0 = 1.225\ \text{kg/m}^3$ and $a_h = 0.14/\ \text{km}$.

The resulting aerodynamic force and moment coefficients as well as the lift-to-drag ratio are shown in Fig. 7 where the blue line denotes the $C_{\tau_y} = 0$ contour. Thus, this line highlights the set of (α, δ) tuples for which the vehicle is at $\dot{q} = 0$, i.e., these are all possible values that the guidance module could specify for the reference angle of attack and elevon deflection. In other words, this line represents all possible values of the lift and drag that are going to act on the vehicle when at $\dot{q} = 0$, thereby providing an insight into the dynamics of the vehicle at a fixed pitch rate. Note that we can potentially change this contour by changing the center of gravity (CG) location of the vehicle. In this work, we use a sixth-order polynomial to fit this $\dot{q} = 0$ contour and utilize the fitted polynomial to generate the reference values (α_r, δ_r) as follows. First, the reference flight path angle is specified through (4). Thus, we can compute the required lift to satisfy the condition in (7). We then use the fitted polynomial to generate a (α_r, δ_r) tuple to satisfy the above mentioned lift requirement. Note that it might not be possible to satisfy the lift requirement in this manner if the required C_L does not fall within the ranges of C_L that correspond to $\dot{q} = 0$. Our future efforts will study the connections between the lift constraint and the set of altitude profiles that guarantees feasible trajectory generation.

We demonstrate the LTV-MPC framework for two cases. In one scenario, the HGV is required to follow a reference altitude profile which includes a pull-up maneuver. The HGV is required to glide at constant dynamic pressure in

the other scenario. The results and the corresponding discussion on these are provided next. For both sets of results, following are some of the parameters related to the LTV-MPC Algorithm 2:

$$\Delta t = 10^{-2}\ \text{s}, N = 10, u_{\min} = -10\ \text{deg}, u_{\max} = 15\ \text{deg}, \mu_s = 0.1, R = 10^6, Q = \text{diag}\left(Q_V, Q_\alpha, Q_\gamma, Q_q\right) \tag{21}$$

where $Q_V = 0.01$, $Q_\alpha = Q_q = R = 10^6$ and $Q_\gamma = 10^9$. Also, the time discretization is carried out through a zero-order hold using the 'c2d' command in MATLAB.

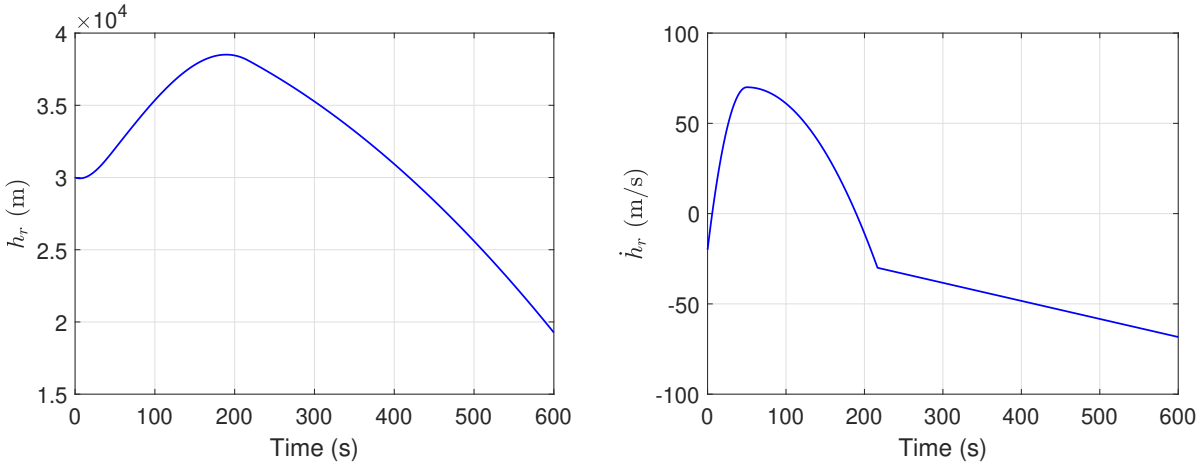

(a) Reference altitude profile **(b) Reference altitude rate profile**

Fig. 8 The reference altitude profile for the HGV prescribing a pull-up maneuver.

A. Reference altitude profile with a pull-up maneuver

In this scenario, the HGV is tasked with flying the reference altitude profile as depicted in Fig. 8, for which the reference altitude rate is specified using two quadratic polynomials in time up to approximately the first 200 seconds.

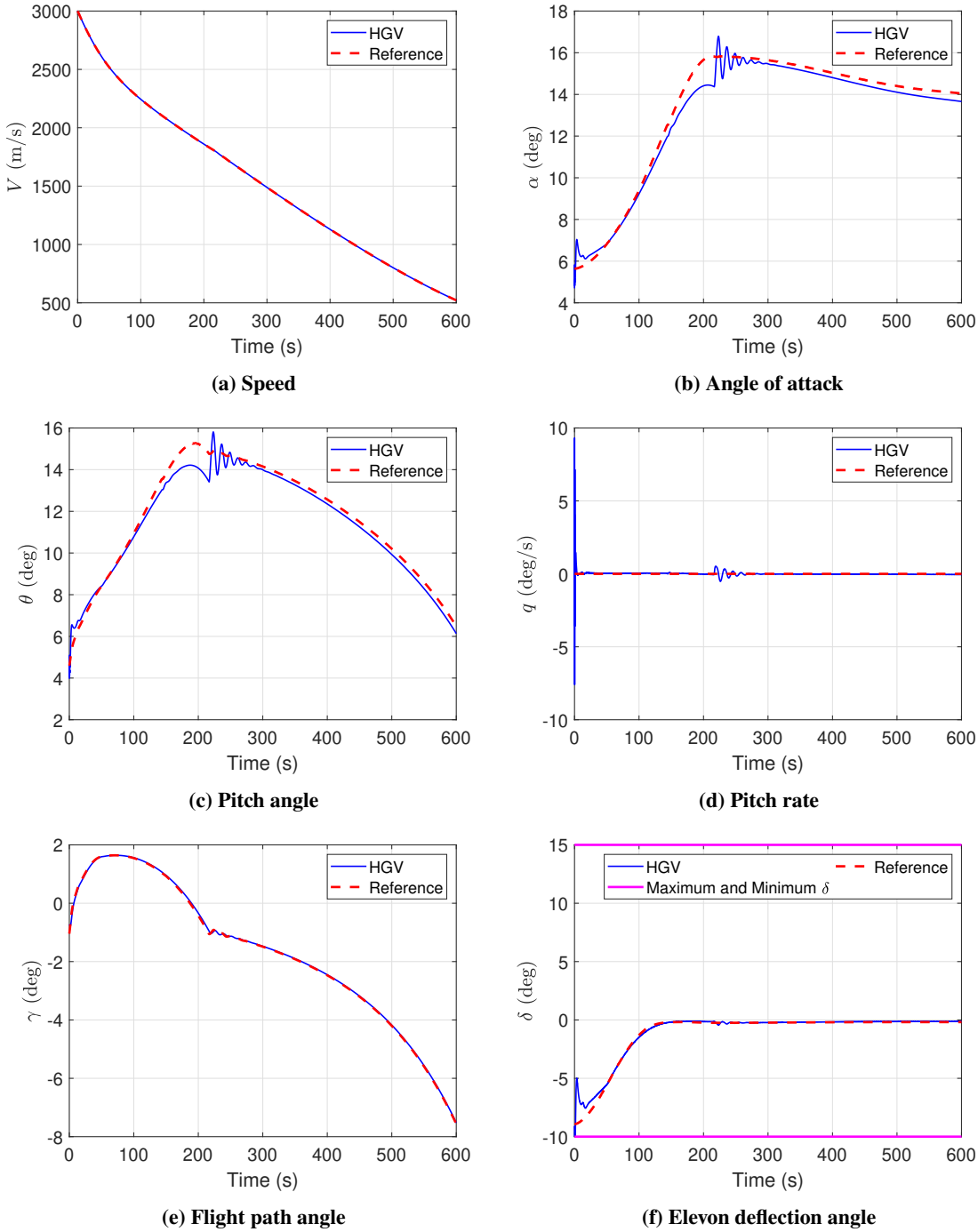

Fig. 9 Closed-loop trajectories of the HGV for the quasi-equilibrium glide using the LTV-MPC framework.

Once the altitude rate drops below -30 m/s, we prescribe a linear rate of drop in the reference altitude rate, as shown in Fig. 8b. Also, the starting altitude is 30 km and the maximum altitude attained through the pull-up is approximately 38.5 km. The quasi-equilibrium reference values at the initial time is computed for this altitude profile with an initial speed of 3 km/s. These are given by

$$\alpha_r(0) = 5.64 \text{ deg}, \gamma_r(0) = -1.04 \text{ deg}, \delta_r(0) = -8.92 \text{ deg} \tag{22}$$

In terms of the reference flight path angle generator in (4), we set $k_1 = 0.2, k_2 = 5$ for the results shown

here. The HGV with the LTV-MPC controller is then randomly initialized around the reference state $x_r(0) = \begin{bmatrix} V_r(0) & \alpha_r(0) & \gamma_r(0) & 0 \end{bmatrix}^{\mathrm{T}}$ with $V_r(0) = 3$ km/s and the angles as shown in (22). The closed-loop state trajectories and the corresponding elevon deflection angle trajectories are shown in Fig. 9. From these results, we observe that the controller makes the HGV track the quasi-equilibrium reference trajectory adequately. Also, these results illustrate nominal robustness of the LTV-MPC setup since the controller—which is based on LTV models—is implemented on the nonlinear HGV dynamics and the HGV tracks the reference trajectory. As the tracking in the flight path angle is adequate, the altitude tracking error reaches a neighborhood of zero within approximately 50 seconds and remains there for the remainder of the flight (see Figs. 10a, 10b). The downrange obtained by flying this altitude profile is as shown in Figs. 10c, 10d.

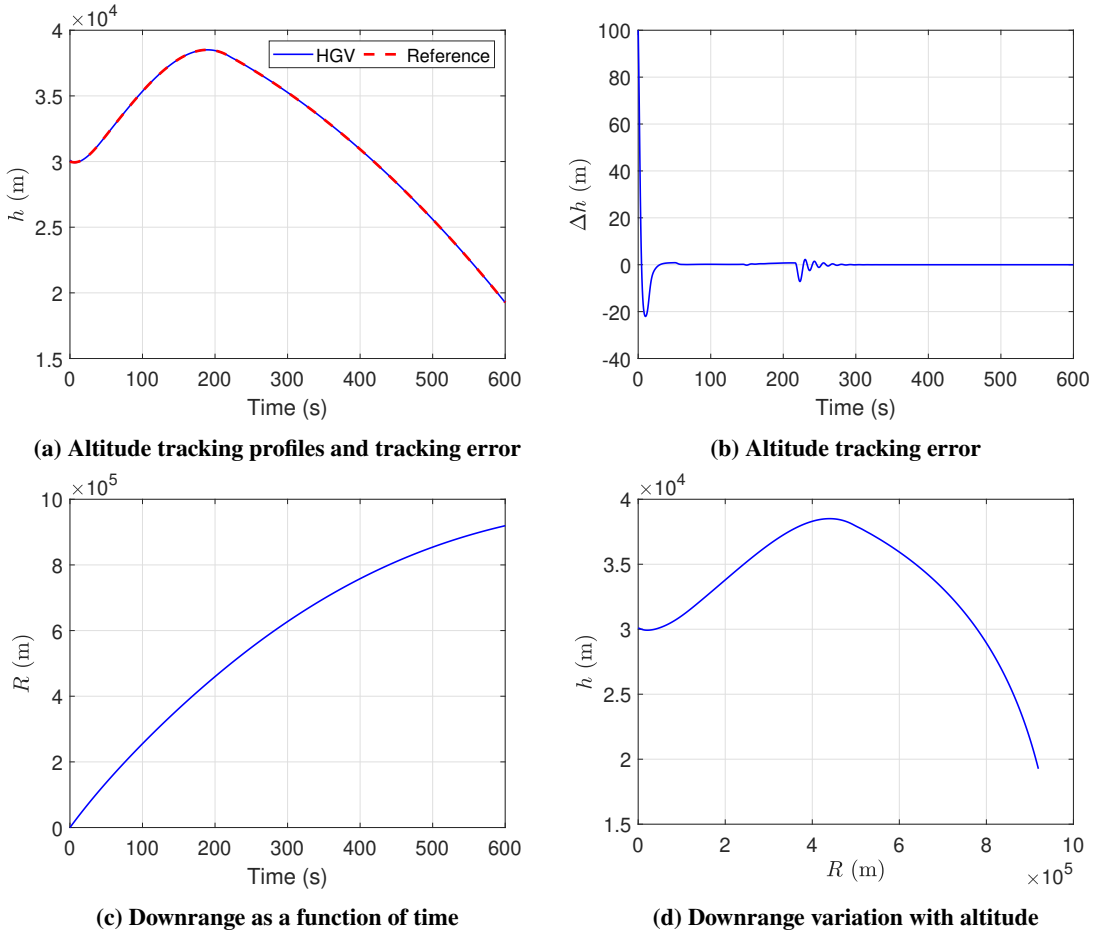

(a) Altitude tracking profiles and tracking error

(b) Altitude tracking error

(c) Downrange as a function of time

(d) Downrange variation with altitude

Fig. 10 The truth and reference altitude profiles, altitude tracking error and downrange profile for the quasi-equilibrium glide using the LTV-MPC framework.

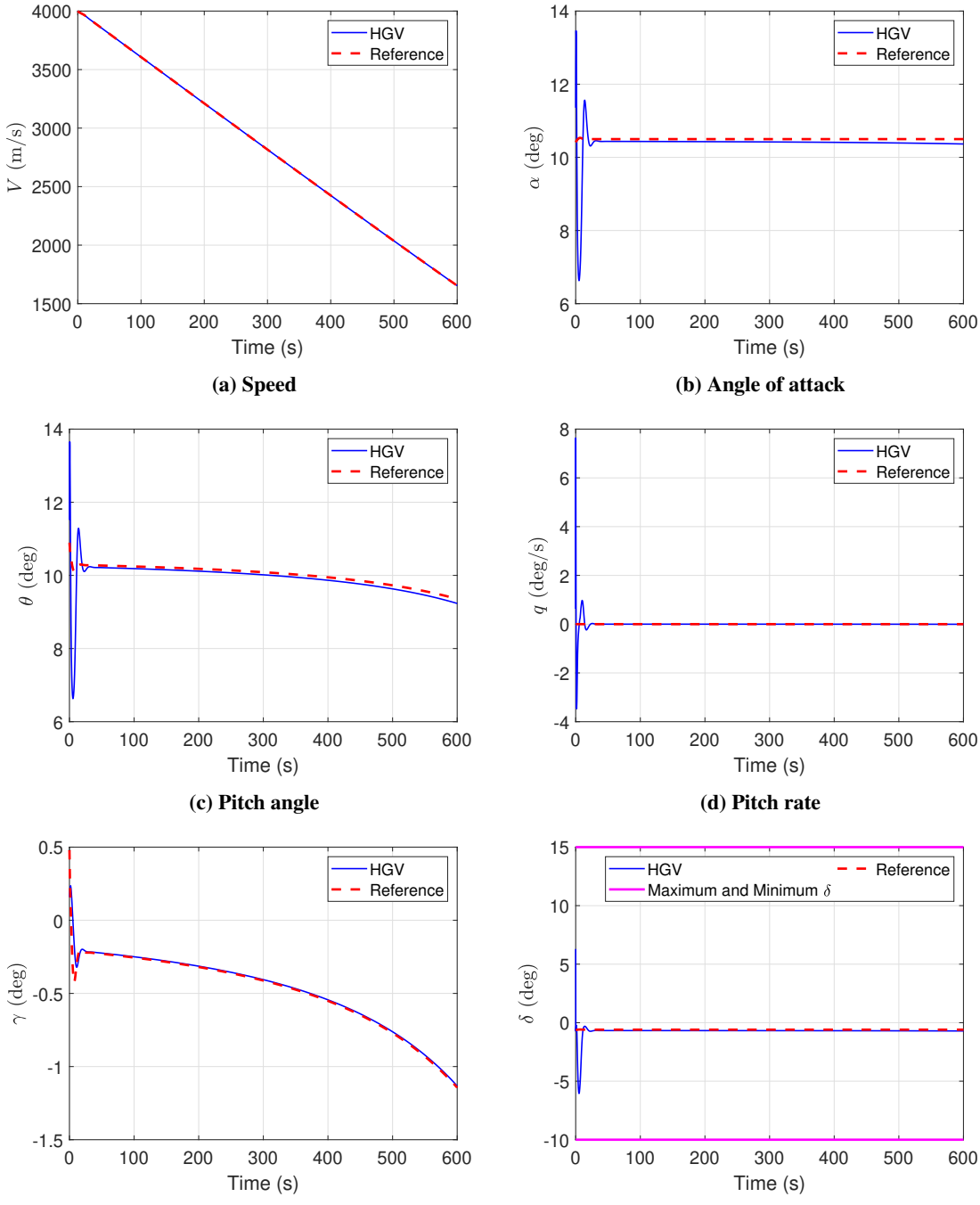

Fig. 11 Closed-loop trajectories of the HGV for the constant dynamic pressure quasi-equilibrium glide using the LTV-MPC framework.

B. Constant dynamic pressure glide

Now, we will consider the case where the HGV is required to fly at a constant dynamic pressure. The reference altitude and altitude rate are generated at every time instant to enforce the constant dynamic pressure constraint as described next. At the current time t, given the reference (constant) dynamic pressure $\bar{Q}_d$ and the current speed $V(t)$, the required atmospheric density to maintain the constant dynamic pressure is given by $\bar{\rho}(t) = \frac{2\bar{Q}_d}{V^2(t)}$. Due to our

above-mentioned assumption of the exponential atmospheric density, we can find the reference altitude to meet this density criteria as

$$h_r(t) = -\frac{1}{a_h} \ln\left(\frac{\bar{\rho}(t)}{\rho_0}\right).$$

Similarly, the reference altitude rate is obtained by differentiating the dynamic pressure and is given by

$$\dot{h}_r(t) = \frac{2\dot{V}(t)}{a_h V(t)}$$

which requires the current acceleration $\dot{V}(t)$ of the HGV. These reference values are then passed on to the integrated guidance and control framework (Algorithm 2) such that the reference dynamic states as well as an elevon deflection angle is synthesized at every time instant.

For the numerical results in this scenario, we select the starting altitude and speed to be 45 km and 4 km/s, respectively, and the reference or constant dynamic pressure corresponds to this altitude and speed. The reference angles at the initial time are

$$\alpha_r(0) = 10.41 \text{ deg}, \gamma_r(0) = 0.47 \text{ deg}, \delta_r(0) = -0.64 \text{ deg} \tag{23}$$

where we have utilized $k_1 = 0.5, k_2 = 1$ for the reference flight path angle generator in (4). The closed-loop trajectories of the HGV states and the elevon deflection angles are shown in Fig. 11. These results again highlight adequate tracking performance of the LTV-MPC controller after the initial transient oscillations. The time history of the dynamic pressure is shown in Fig. 12a and we can conclude that the integrated guidance and control framework is able to fly the HGV at the specified, constant dynamic pressure.

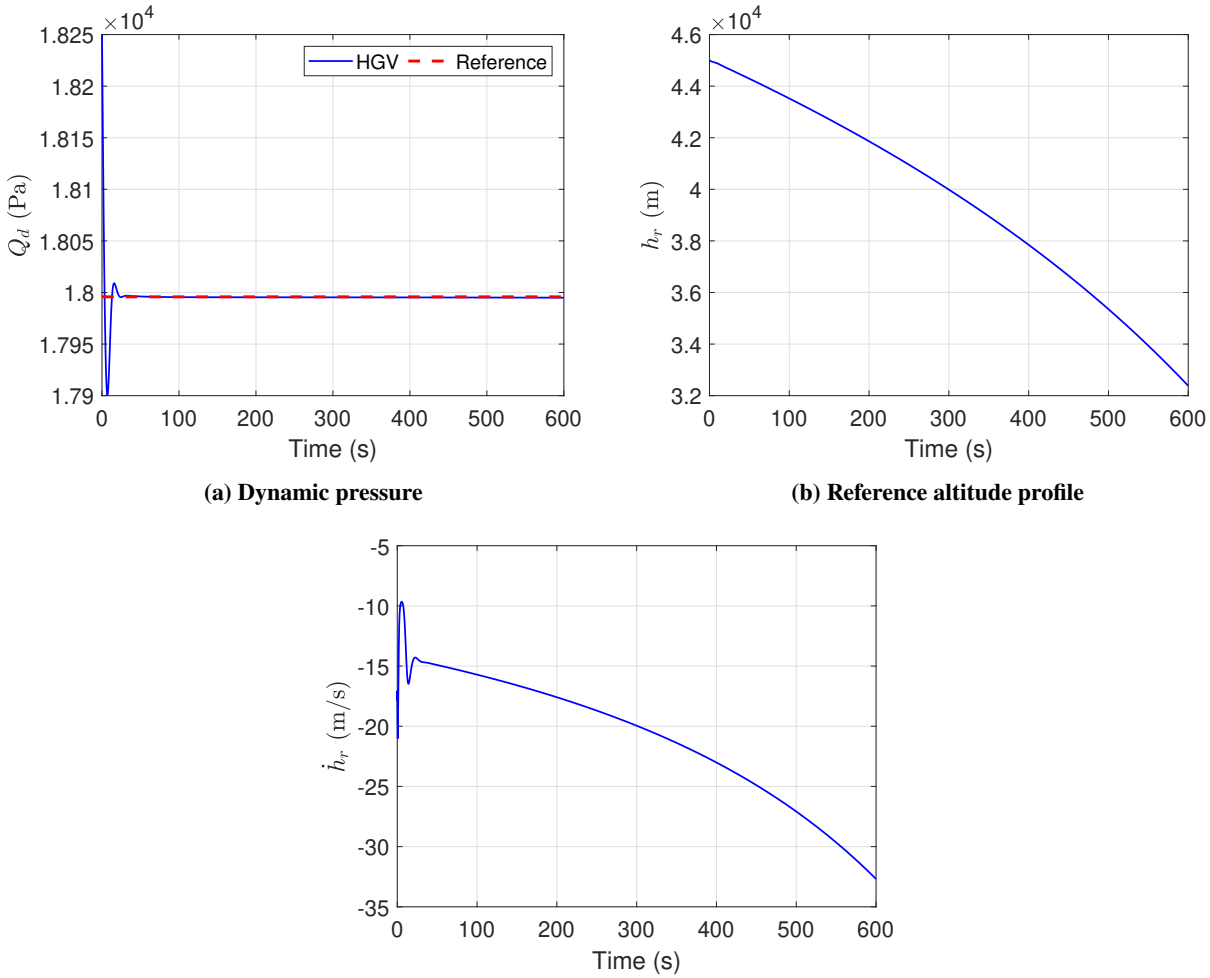

(a) Dynamic pressure

(b) Reference altitude profile

(c) Reference altitude rate profile

Fig. 12 The dynamic pressure history, along with the associated reference altitude and altitude rate profiles, of the HGV for the constant dynamic pressure glide.

Also, the entire reference altitude profile and altitude rate—obtained by enforcing the constant dynamic pressure constraint as described above—are shown in Fig. 12. Since the dynamic pressure is kept constant, the reference angle of attack and deflection angles do not vary much over the duration of the flight as the C_L to satisfy the lift requirement in (7) remains almost constant throughout the flight after the initial transient behavior. The altitude profile of the HGV and the reference altitude profile, along with the altitude tracking error, are shown in Figs. 13a, 13b. As shown in Fig. 13b, the altitude tracking error converges close to zero in approximately 20 seconds and remains there for the remainder of the flight. Note that this is a result of the adequate tracking in the flight path angle (see Fig. 11e). The downrange obtained by flying at constant dynamic pressure is as shown in Figs. 13c, 13d. The downrange obtained in this case is significantly higher compared to the last case and that is primarily due to the flight path angle remaining fairly close to zero over the entire flight compared to the case with the pull-up maneuver (compare results in Fig. 9e and Fig. 11e).

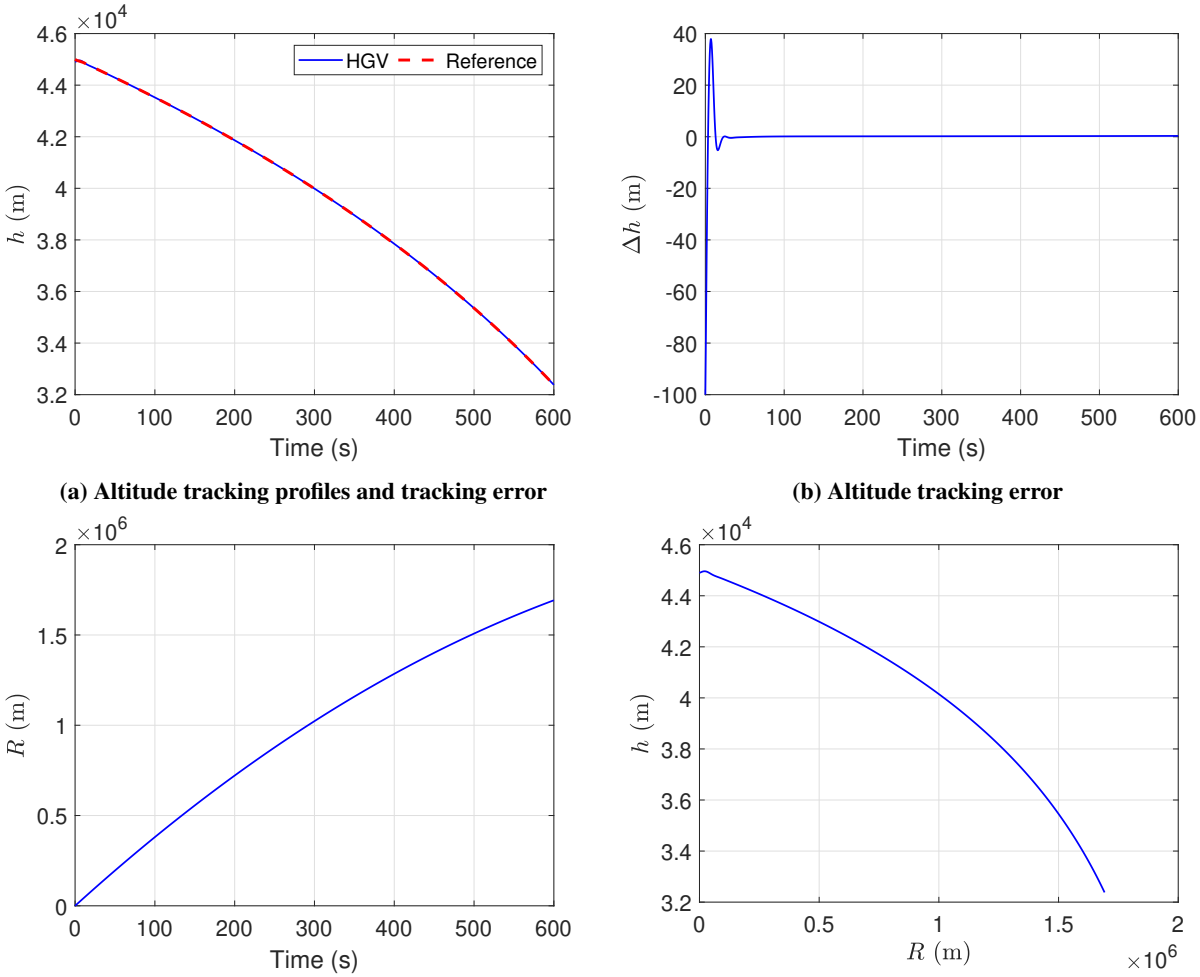

(a) Altitude tracking profiles and tracking error

(b) Altitude tracking error

(c) Downrange as a function of time

(d) Downrange variation with altitude

Fig. 13 The truth and specified (reference) altitude profiles, altitude tracking error, and downrange profiles for the constant dynamic pressure glide using the LTV-MPC framework.

V. Conclusion and Future Work

The current work has developed a LTV-MPC setup to be used in the analysis of relevant hypersonic geometries with control surfaces. This research supports ongoing efforts at the University of Minnesota to create tools for hypersonic vehicle analysis, specifically accounting for the effects of control surfaces. The primary objective of this research is not to design an optimized HGV or controller for a specific geometry but to develop an analysis tool that facilitates the rapid exploration of design spaces for complex hypersonic geometries. Advancements in grid-generation frameworks, such as those by Drayna et al. [13], Bartkowcz et al. [14], have enabled the efficient creation and meshing of parametrically defined geometries. These frameworks also support interpolation between meshes to simulate control surface deflections. Thereby enabling the rapid generation of high-fidelity CFD flow fields over extensive design spaces. As a result, several thousand steady-state flow fields were generated to build an aerodynamic database that informed the MPC framework. The data indicate that dynamic pressure scaling provides good agreement for aerodynamic forces and moments at modest angles of attack and control surface deflections. However, at larger angles, boundary layer separation, transition to turbulence, or other flow instabilities mechanisms may cause inaccuracies in this approach.

Future research will focus on improving the interpolation methods for the aerodynamic database, including exploring direct interpolation of flow fields rather than the derived aerodynamic quantities. Additionally, the MPC framework will be implemented in a closed-loop system with CFD, replacing the current data-driven approximations with real-time aerodynamic computations. This allows the added benefit of accurately representing the integrated heating throughout

the vehicle's trajectory with conjugate heat transfer.

At the conclusion of these efforts, it is the goal of this research to demonstrate the integration of these frameworks for optimizing a parametrically defined hypersonic glide vehicle, accounting for aerodynamic shape, trajectory, controls, and their interactions, thereby providing a robust tool for hypersonic vehicle design and analysis.

Acknowledgments

This work was supported by the Air Force Office of Scientific Research under grant number FA9550-1-22-0004. The views and conclusions contained herein are those of the authors and should be not interpreted as representing the official policies or endorsements, either expressed or implied, of the AFOSR or the U.S. Government.

References

[1] Mirmirani, M., Wu, C., Clark, A., Choi, S. B., and Colgren, R., *Modeling for Control of a Generic Airbreathing Hypersonic Vehicle*, 2005. doi:10.2514/6.2005-6256, URL https://arc.aiaa.org/doi/abs/10.2514/6.2005-6256.

[2] Yu, W., and Chen, W., "Guidance scheme for glide range maximization of a hypersonic vehicle," *AIAA Guidance, navigation, and control conference*, 2011, p. 6714.

[3] Shin, J., "Adaptive dynamic surface control for a hypersonic aircraft using neural networks," *IEEE Transactions on Aerospace and Electronic Systems*, Vol. 53, No. 5, 2017, pp. 2277–2289.

[4] Xu, H., Mirmirani, M. D., and Ioannou, P. A., "Adaptive sliding mode control design for a hypersonic flight vehicle," *Journal of guidance, control, and dynamics*, Vol. 27, No. 5, 2004, pp. 829–838.

[5] Parker, J. T., Serrani, A., Yurkovich, S., Bolender, M. A., and Doman, D. B., "Control-oriented modeling of an air-breathing hypersonic vehicle," *Journal of Guidance, Control, and Dynamics*, Vol. 30, No. 3, 2007, pp. 856–869.

[6] Fiorentini, L., Serrani, A., Bolender, M. A., and Doman, D. B., "Nonlinear robust adaptive control of flexible air-breathing hypersonic vehicles," *Journal of guidance, control, and dynamics*, Vol. 32, No. 2, 2009, pp. 402–417.

[7] Lu, P., and Hanson, J. M., "Entry guidance for the X-33 vehicle," *Journal of Spacecraft and Rockets*, Vol. 35, No. 3, 1998, pp. 342–349.

[8] Shen, Z., and Lu, P., "Onboard generation of three-dimensional constrained entry trajectories," *Journal of Guidance, control, and Dynamics*, Vol. 26, No. 1, 2003, pp. 111–121.

[9] Lu, P., "Entry guidance: a unified method," *Journal of Guidance, Control, and Dynamics*, Vol. 37, No. 3, 2014, pp. 713–728.

[10] Roenneke, A. J., and Cornwell, P. J., "Trajectory control for a low-lift re-entry vehicle," *Journal of Guidance, Control, and Dynamics*, Vol. 16, No. 5, 1993, pp. 927–933.

[11] Lu, P., "Regulation about time-varying trajectories: precision entry guidance illustrated," *Journal of Guidance, Control, and Dynamics*, Vol. 22, No. 6, 1999, pp. 784–790.

[12] Shou, Y., Yan, T., Xu, B., and Sun, F., "Integrated guidance and control of hypersonic flight vehicle with coordinated mission requirement and input constraint," *International Journal of Robust and Nonlinear Control*, Vol. 33, No. 7, 2023, pp. 4262–4280.

[13] Drayna, T. W., Stam, H. R., , Long, L. J., Lang, L. M., and Pate, J. P., "Crosslink V.0.11.x User Manual," 2022. doi: 10.2172/1888178, URL https://www.osti.gov/biblio/1888178.

[14] Bartkowcz, M., Haag, C., Nitzkorski, Z., Gidzak, V., and Brock, J., "LINK3D - Grid generation software overview and application," 2023.

[15] Candler, G. V., Johnson, H. B., Nompelis, I., Gidzak, V. M., Subbareddy, P. K., and Barnhardt, M., "Development of the US3D code for advanced compressible and reacting flow simulations," *53rd AIAA Aerospace Sciences Meeting*, 2015. doi:10.2514/6.2015-1893.

[16] Nompelis, I., Drayna, T., and Candler, G., *Development of a Hybrid Unstructured Implicit Solver for the Simulation of Reacting Flows Over Complex Geometries*, 2012. doi:10.2514/6.2004-2227, URL https://arc.aiaa.org/doi/abs/10.2514/6.2004-2227.

[17] *U.S. Standard Atmosphere, 1976*, 1976. URL https://ntrs.nasa.gov/api/citations/19770009539/downloads/19770009539.pdf.

[18] Slotine, J.-J. E., Li, W., et al., *Applied nonlinear control*, Prentice hall Englewood Cliffs, NJ, 1991.

[19] Xu, R., and Ozguner, U., "Sliding mode control of a quadrotor helicopter," *Proceedings of the 45th IEEE Conference on Decision and Control*, IEEE, 2006, pp. 4957–4962.

[20] Ru, P., and Subbarao, K., "Nonlinear model predictive control for unmanned aerial vehicles," *Aerospace*, Vol. 4, No. 2, 2017.

[21] Falcone, P., Tufo, M., Borrelli, F., Asgari, J., and Tseng, H. E., "A linear time varying model predictive control approach to the integrated vehicle dynamics control problem in autonomous systems," *2007 46th IEEE conference on decision and control*, IEEE, 2007, pp. 2980–2985.

[22] Falcone, P., Borrelli, F., Tseng, H. E., Asgari, J., and Hrovat, D., "Linear time-varying model predictive control and its application to active steering systems: Stability analysis and experimental validation," *International Journal of Robust and Nonlinear Control*, Vol. 18, No. 8, 2008, pp. 862–875.

[23] Knutson, A., GS, S., and Candler, G. V., "Direct numerical simulation of mach 6 flow over a cone with a highly swept fin," *2018 AIAA Aerospace Sciences Meeting*, 2018. doi:10.2514/6.2018-0379.